The Astrophysical Journal, 740:86 (9pp), 2011 October 20 doi:10.1088/0004-637X/740/2/86

THE ATACAMA COSMOLOGY TELESCOPE: CALIBRATION WITH THE *WILKINSON MICROWAVE ANISOTROPY PROBE* USING CROSS-CORRELATIONS

Amir Hajian[1,2,3], Viviana Acquaviva[2,4], Peter A. R. Ade[5], Paula Aguirre[6], Mandana Amiri[7], John William Appel[3], L. Felipe Barrientos[6], Elia S. Battistelli[7,8], John R. Bond[1], Ben Brown[9], Bryce Burger[7], Jay Chervenak[10], Sudeep Das[2,3,11], Mark J. Devlin[12], Simon R. Dicker[12], W. Bertrand Doriese[13], Joanna Dunkley[2,3,14], Rolando Dünner[3], Thomas Essinger-Hileman[3], Ryan P. Fisher[3], Joseph W. Fowler[3], Mark Halpern[7], Matthew Hasselfield[7], Carlos Hernández-Monteagudo[15], Gene C. Hilton[13], Matt Hilton[16,17], Adam D. Hincks[3], Renée Hlozek[14], Kevin M. Huffenberger[18], David H. Hughes[19], John P. Hughes[4], Leopoldo Infante[6], Kent D. Irwin[13], Jean Baptiste Juin[6], Madhuri Kaul[12], Jeff Klein[12], Arthur Kosowsky[9], Judy M. Lau[3,20,21], Michele Limon[3,12,22], Yen-Ting Lin[2,6,23], Robert H. Lupton[2], Tobias A. Marriage[2,24], Danica Marsden[12], Phil Mauskopf[5], Felipe Menanteau[4], Kavilan Moodley[16,17], Harvey Moseley[10], Calvin B. Netterfield[25], Michael D. Niemack[3,13], Michael R. Nolta[1], Lyman A. Page[3], Lucas Parker[3], Bruce Partridge[26], Beth Reid[3,27], Neelima Sehgal[20], Blake D. Sherwin[3], Jon Sievers[1], David N. Spergel[2], Suzanne T. Staggs[3], Daniel S. Swetz[12,13], Eric R. Switzer[3,28], Robert Thornton[12,29], Hy Trac[2,30], Carole Tucker[5], Ryan Warne[16], Ed Wollack[10], and Yue Zhao[3]

[1] Canadian Institute for Theoretical Astrophysics, University of Toronto, Toronto, ON M5S 3H8, Canada
[2] Department of Astrophysical Sciences, Peyton Hall, Princeton University, Princeton, NJ 08544, USA
[3] Joseph Henry Laboratories of Physics, Jadwin Hall, Princeton University, Princeton, NJ 08544, USA
[4] Department of Physics and Astronomy, Rutgers, The State University of New Jersey, Piscataway, NJ 08854-8019, USA
[5] School of Physics and Astronomy, Cardiff University, The Parade, Cardiff, Wales CF24 3AA, UK
[6] Departamento de Astronomía y Astrofísica, Facultad de Física, Pontificía Universidad Católica de Chile, Casilla 306, Santiago 22, Chile
[7] Department of Physics and Astronomy, University of British Columbia, Vancouver, BC V6T 1Z4, Canada
[8] Department of Physics, University of Rome "La Sapienza," Piazzale Aldo Moro 5, I-00185 Rome, Italy
[9] Department of Physics and Astronomy, University of Pittsburgh, Pittsburgh, PA 15260, USA
[10] Code 553/665, NASA/Goddard Space Flight Center, Greenbelt, MD 20771, USA
[11] Berkeley Center for Cosmological Physics, LBL and Department of Physics, University of California, Berkeley, CA 94720, USA
[12] Department of Physics and Astronomy, University of Pennsylvania, Philadelphia, PA 19104, USA
[13] NIST Quantum Devices Group, Boulder, CO 80305, USA
[14] Department of Astrophysics, Oxford University, Oxford OX1 3RH, UK
[15] Max Planck Institut für Astrophysik, D-85741 Garching bei München, Germany
[16] Astrophysics and Cosmology Research Unit, School of Mathematical Sciences, University of KwaZulu-Natal, Durban 4041, South Africa
[17] Centre for High Performance Computing, CSIR Campus, Cape Town, South Africa
[18] Department of Physics, University of Miami, Coral Gables, FL 33124, USA
[19] Instituto Nacional de Astrofísica, Óptica y Electrónica (INAOE), Tonantzintla, Puebla, Mexico
[20] Kavli Institute for Particle Astrophysics and Cosmology, Stanford University, Stanford, CA 94305-4085, USA
[21] Department of Physics, Stanford University, Stanford, CA 94305-4085, USA
[22] Columbia Astrophysics Laboratory, New York, NY 10027, USA
[23] Institute for the Physics and Mathematics of the Universe, The University of Tokyo, Kashiwa, Chiba 277-8568, Japan
[24] Department of Physics and Astronomy, The Johns Hopkins University, Baltimore, MD 21218-2686, USA
[25] Department of Physics, University of Toronto, Toronto, ON M5S 1A7, Canada
[26] Department of Physics and Astronomy, Haverford College, Haverford, PA 19041, USA
[27] ICREA & Institut de Ciencies del Cosmos (ICC), University of Barcelona, Barcelona 08028, Spain
[28] Kavli Institute for Cosmological Physics, Laboratory for Astrophysics and Space Research, Chicago, IL 60637, USA
[29] Department of Physics, West Chester University of Pennsylvania, West Chester, PA 19383, USA
[30] Harvard-Smithsonian Center for Astrophysics, Harvard University, Cambridge, MA 02138, USA
Received 2010 August 13; accepted 2011 July 23; published 2011 October 3

ABSTRACT

We present a new calibration method based on cross-correlations with the *Wilkinson Microwave Anisotropy Probe* (*WMAP*) and apply it to data from the Atacama Cosmology Telescope (ACT). ACT's observing strategy and map-making procedure allows an unbiased reconstruction of the modes in the maps over a wide range of multipoles. By directly matching the ACT maps to *WMAP* observations in the multipole range of $400 < l < 1000$, we determine the absolute calibration with an uncertainty of 2% in temperature. The precise measurement of the calibration error directly impacts the uncertainties in the cosmological parameters estimated from the ACT power spectra. We also present a combined map based on ACT and *WMAP* data that has a high signal-to-noise ratio over a wide range of multipoles.

Key words: cosmic background radiation – cosmology: observations – methods: data analysis – methods: statistical

Online-only material: color figures

1. INTRODUCTION

Observations of the cosmic microwave background (CMB) are one of the key probes of cosmology. Current balloon- and ground-based measurements (Sayers et al. 2009; Brown et al. 2009; Friedman et al. 2009; Reichardt et al. 2009a, 2009b; Sharp et al. 2010; Dawson et al. 2006; Sievers et al. 2009; Lueker et al. 2009; Fowler et al. 2010) and space-based

experiments (Komatsu et al. 2011) measure the amplitude of CMB fluctuations over a wide range of angular scales. All-sky maps of the *Wilkinson Microwave Anisotropy Probe* (*WMAP*) provide a large-scale measurement of the CMB with only a 0.2% calibration uncertainty (Jarosik et al. 2011). The scientific value of the small-scale ground- and balloon-based measurements are maximized if these precise small-scale maps can be accurately calibrated to *WMAP*.

Starting with the comparisons between FIRS and *COBE* (Ganga et al. 1993), cross-calibration studies have both confirmed detections and provided common calibration between experiments. General methods for cross-calibration have been developed for CMB studies (Ganga et al. 1993; Tegmark 1999) and applied to many different experiments: Reichardt et al. (2009a, ACBAR with *WMAP*), Brown et al. (2009, QUaD with BOOMERANG), Chiang et al. (2010, BICEP with *WMAP*), Xu et al. (2001, SASK and QMAP with *COBE*), Netterfield et al. (1997, SASK with MSAM), Abroe et al. (2004, Maxima with *WMAP*), Hernández-Monteagudo et al. (2006, ARCHEOPS and *WMAP*), and Masi et al. (2006, BOOMERANG and *WMAP*). An alternative approach to calibration relies on measuring known point sources, particularly planets. This approach has also been used by many CMB experiments (Crill et al. 2003; Mason et al. 2003) and is applied in Section 2.2.

We present a new method based on cross-correlations with *WMAP* to accurately measure the absolute calibration uncertainty for Atacama Cosmology Telescope (ACT) observations. The method we present here expands on earlier work in that we take full advantage of working in Fourier space. The Fourier space algorithms introduced in this paper are fast and simple. Filtering noisy modes, deconvolving the beam, and estimating the anisotropic noise model are faster and easier in Fourier space. The *WMAP* map uses co-added inverse-noise weighted data from seven single-year maps and four differencing assemblies at 94 GHz.[31] In normalizing to *WMAP*, we assume that the fluctuations in the sky are statistically isotropic. This is a plausible assumption that can be tested within the *WMAP* data (Hajian & Souradeep 2006; Bennett et al. 2011).

The ACT data used in this paper were collected at 148 GHz and 218 GHz during the 2008 observing season. The maps are solved for iteratively using a preconditioned conjugate gradient code to obtain the unbiased maximum likelihood solution. For an overview of the ACT data reduction pipeline, we refer the reader to Fowler et al. (2010) and Dünner (2009). For the power spectrum results and cosmological parameters, see the companion papers (Das et al. 2011; Dunkley et al. 2011), and for clusters using the Sunyaev–Zel'dovich effect (Sunyaev & Zel'dovich 1970) see Marriage et al. (2011a), Menanteau et al. (2010), and Sehgal et al. (2011). For information on the telescope facility, see Fowler et al. (2007), Hincks et al. (2008), Switzer et al. (2008) and Swetz et al. (2011). Details of the cryogenic receiver and bolometric detectors are provided in Niemack (2006), Marriage et al. (2006), Fowler et al. (2007), Battistelli et al. (2008), Niemack et al. (2008), Swetz et al. (2008), Thornton et al. (2008), and Zhao et al. (2008).

In Section 2 we briefly describe the data sets used for this analysis. In Section 3 we present a cross-correlation method to test the relative alignment of the ACT maps versus *WMAP* maps. Our calibration method is discussed in Section 4. Section 5 presents our combined high-resolution CMB map that is signal-to-noise dominated over a wide range of multipoles ($l < 5000$).

[31] from http://lambda.gsfc.nasa.gov

2. DATA

The cross-correlation method used in this paper requires a single map from *WMAP* and four maps with independent noise properties from ACT at each frequency. Below we give a brief description of the three data sets that are used in this paper. Throughout this paper we use a to denote ACT data and w to denote *WMAP* data.

2.1. ACT Data

One of the strengths of ACT is its scanning strategy. The geographical location of the ACT telescope (the Atacama Desert) enables cross-linking of observations. Every observing region is scanned along two different directions at constant elevation each night. Azimuth-only scans observe a sky field at the same elevation twice a night: once as the field rises, once as it sets. Sky rotation changes the scan angle, resulting in cross-linking, which allows (in principle) the reconstruction of all the modes in the map. The modes that are lost due to the correlated noise along the scan direction in the rising maps are won back using the setting maps and vice versa. Such cross-linking and the unbiased map-making algorithm used to make ACT maps yield a successful reconstruction of the modes in the maps down to multipoles of ∼300. The combination of ACT's scan strategy and its unbiased map-making scheme enables a direct calibration to *WMAP*. However, since *WMAP* is noisy on small scales and ACT's maps are dominated by atmospheric noise and poorly measured modes on its largest scales, our method compares the maps as a function of multipole over the $400 < l < 1000$ range.

The ACT maps used in this paper are identical to the maps used in Das et al. (2011). The area includes that in Fowler et al. (2010) and represents the highest sensitivity data from 2008 (148 GHz and 218 GHz). The map resolution is 1.′4 and 1.′0 at 148 GHz and 218 GHz, respectively (Hincks et al. 2010). The map projection used is a cylindrical equal area with square pixels, 0.′5 on a side. We divide the data into 12 patches. Each patch is $5^\circ \times 5^\circ$ in size, and together they cover a rectangular area of the map from $\alpha = 00^{\rm h}22^{\rm m}$ to $06^{\rm h}52^{\rm m}$ (5.°5 to 103°) in right ascension and from $\delta = -55^\circ$ to -50° in declination. We divide our data set into four equal subsets in time, such that the four independent maps generated from these subsets cover the same area and have similar depths. Therefore, for each patch described above we have four maps, each representing roughly a quarter of the time spent on that patch. We call these "season maps." The length elements in the map are given by $dy = \delta_{\rm DEC}$ and $dx = \delta_{\rm RA} \cos {\rm DEC}$, in y and x directions, respectively, where DEC is the average declination in the region of interest. Figure 1 shows the ACT region used in this analysis.

2.2. Calibration to Planets

Observations of Uranus provide the initial calibration of the maps. Uranus was observed by ACT every few days during the 2008 season, yielding approximately 30 usable observations. The time-ordered data from each observation are calibrated to detector power units and a map is produced. From each map, the peak response of the planet is determined, corrected for the temperature dilution due to the finite instrumental beam size (i.e., by multiplying by the ratio of Uranus's solid angle to the instrumental beam solid angle) and then compared to the Uranus temperature (converted to CMB differential units) at the band effective frequency. The calibration factors from detector power units to CMB differential temperature are compared to precipitable water vapor (PWV) measurements to fit a model

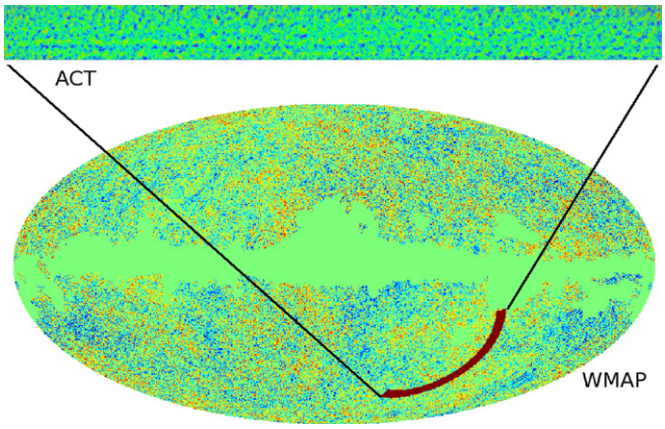

Figure 1. ACT and *WMAP* maps used in this paper. The red region in the *WMAP* map shows the overlap between *WMAP* and the ACT data.

(A color version of this figure is available in the online journal.)

of atmospheric opacity, and the season map calibration factor is obtained by evaluating the fit at the season mean PWV of 0.5. The uncertainty in the Uranus-based calibration is 7%, and is dominated by the 5% uncertainty in the planet's temperature.

We take the brightness temperature[32] of Uranus to be 107 ± 6 K and 96 ± 6 K for the 148 GHz and 218 GHz bands, respectively. These temperatures are based on a reprocessing of the data presented by Griffin & Orton (1993), in combination with *WMAP* seven-year measurements of Mars and Uranus brightnesses (Weiland et al. 2011). Griffin & Orton measured flux ratios between Uranus and Mars at several wavelengths from 350 μm to 1.9 mm. These were calibrated to absolute units using an extrapolation of the Wright model (Wright 1976) for Mars temperature, and the resulting Uranus brightness temperatures were fit with a third-order polynomial in the logarithm of the wavelength. We have followed the same procedure, but with two modifications. The first is that the *WMAP* measurements of Uranus temperature at 94, 61, and 41 GHz have been included in the fit. The second is that the *WMAP* comparison of Mars temperature at 94 GHz (3.2 mm) to the Wright model at 350 μm is used to pin the long-wavelength end of the Mars brightness extrapolation. The resulting Uranus brightness temperatures in the two bands are 5% and 3% lower than those obtained by Griffin & Orton. This difference is due almost entirely to the recalibration of the Mars model.

2.3. WMAP Data

The *WMAP* map uses co-added inverse-noise weighted data from seven single-year maps and four differencing assemblies at 94 GHz.[33] The maps are foreground cleaned (using the foreground template model discussed in Hinshaw et al. 2007) and are at HEALPix[34] resolution 10 ($N_{\rm side}$ = 1024), with 3.′5 pixels. Single-year maps are multiplied by the pixel weights based on pixel noise evaluated with the expression

$$\sigma^2(\boldsymbol{n}) = \sigma_W^2 \big/ N_{\rm obs}, \qquad (1)$$

where $N_{\rm obs}$ is the number of observations at each map pixel which is directly proportional to the statistical weight and σ_W is the noise for each differencing assembly. The four noise factors in mK units are given in Table 1.

[32] Throughout, the *brightness temperature* refers to the temperature of a blackbody having the observed in-band spectral radiance. The equivalent *Rayleigh–Jeans temperatures* of Uranus for our bands are 103.5 and 90.7 K.

[33] from http://lambda.gsfc.nasa.gov

[34] http://healpix.jpl.nasa.gov

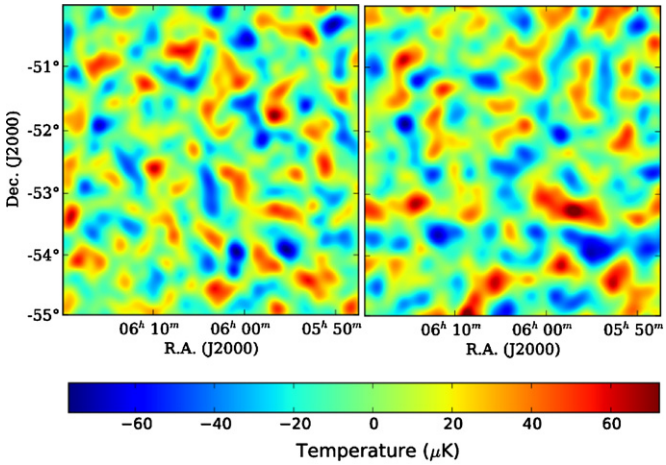

Figure 2. One of the twelve patches used for cross-correlations from ACT 148 GHz (right) and *WMAP* data (left). Long-wavelength modes have been removed from both maps using the high-pass filter described in Equation (2). The ACT map has been convolved with the *WMAP W*-band beam. The two maps represent the same area in the sky, observed by two experiments. The similarity between structures in the two maps is the key feature that we use for our cross-correlation studies. The ACT maps have large-scale atmospheric noise and the *WMAP* maps are dominated by detector noise on the smallest scales. These two types of noise are completely uncorrelated.

(A color version of this figure is available in the online journal.)

Table 1
The rms Noise for Each *WMAP* Differencing Assembly

σ	W_1	W_2	W_3	W_4
σ_W(mK)	5.906	6.572	6.941	6.778

We cut a rectangular region from the resulting HEALPix map corresponding to the ACT southern strip and project it onto the cylindrical equal area coordinates. Both the *WMAP* and ACT data are cut into the same 12 patches. Figure 2 shows one of these patches and the corresponding patch from the ACT measurements. While both maps show similar hot and cold spots, the *WMAP* beam has smoothed out small-scale structure and the ACT maps contain large-scale atmospheric noise.

Because the ACT maps have poorly measured modes on the largest scales, the *WMAP* and ACT maps are filtered by a high-pass filter $F_c(l)$ in Fourier space before being cut into 12 patches. The high-pass filter is a smooth sine-squared function in Fourier space given by

$$F_c(l) = \sin^2 x(l)\Theta(l - l_{\rm min})\Theta(l_{\rm max} - l) + \Theta(l - l_{\rm max}), \qquad (2)$$

where $x(l) = (\pi/2)(l - l_{\rm min})/(l_{\rm max} - l_{\rm min})$ and Θ is the Heavyside function. We choose $l_{\rm min} = 100$ and $l_{\rm max} = 500$. The final power spectrum is corrected for this filter as well as for the effects of the beam and pixel window functions.

3. COMPARING MAPS

We test the alignment of the maps by computing their real-space cross-correlation function as a function of offset $\boldsymbol{x}$. This is done by inverse Fourier transforming the two-dimensional cross-correlation in Fourier space:

$$M_{a\times w}(\boldsymbol{x}) = \sum_{\boldsymbol{l}} \tilde{a}(\boldsymbol{l})\tilde{w}^*(\boldsymbol{l}) \exp(i\boldsymbol{l}\cdot\boldsymbol{x}). \qquad (3)$$

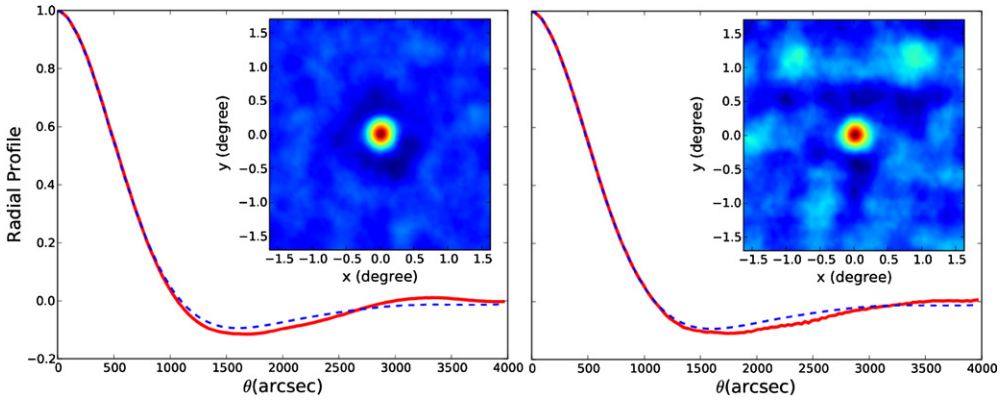

Figure 3. Comparing ACT and *WMAP* data sets: two-dimensional cross-correlations of *WMAP* and ACT maps in real space (inset panels) and their one-dimensional radial profiles (solid red curves) for the 148 GHz maps (left) and 218 GHz maps (right). Two-dimensional cross-correlations peak at zero lag. This solidifies that the maps are aligned and the pointing agrees on average over the whole map area. Results obtained from the noiseless simulations of Sehgal et al. (2010) are also plotted (dashed blue lines). The data correlation functions agree with the simulations. A $\sigma = 7.'7$ Gaussian profile is a good fit to the two-dimensional correlations at small scales ($<10'$).

(A color version of this figure is available in the online journal.)

Here $a(\boldsymbol{l})$ and $w(\boldsymbol{l})$ are the Fourier transforms of the ACT and *WMAP* maps, respectively, and the tilde denotes high-pass filtering of those maps, $\tilde{a}(\boldsymbol{l}) = a(\boldsymbol{l})F_c(\boldsymbol{l})$ and $\tilde{w}(\boldsymbol{l}) = w(\boldsymbol{l})F_c(\boldsymbol{l})$. The high-pass filtering is important here because otherwise long-wavelength noisy modes dominate the cross-correlation and hide the true signal. The resulting two-dimensional cross-correlation function, $M_{a\times w}$, can be written as

$$M_{a\times w}(\boldsymbol{x}) = C(\boldsymbol{x}) \otimes B(\boldsymbol{x}) + n(\boldsymbol{x}), \quad (4)$$

where $B(\boldsymbol{x})$ is an effective beam between the two maps, $C(\boldsymbol{x})$ is the correlation function of the two sky maps, and $n(\boldsymbol{x})$ is the noise fluctuations in the cross-correlation that gets smaller as we add more area. For a perfectly aligned pair of maps, the two-dimensional cross-correlation function, $M_{a\times w}(\boldsymbol{x})$, peaks at $\boldsymbol{x} = 0$ and its width is determined by the correlation length of the field and the beams. For our maps, the result of this is shown in Figure 3. The cross-correlation function is cleanly peaked at zero lag, which shows the maps are aligned and correlated. The noiseless sky simulations of Sehgal et al. (2010) provide a confirmation of these results. We convolve the simulated maps with the *WMAP* and ACT beams to generate simulated noiseless maps of *WMAP* and ACT data, respectively. The maps are then filtered with the high-pass filter of Equation (2) and cut into 12 patches. The real-space cross-correlation of the simulated maps is computed using Equation (4). The result is plotted in Figure 3 (dashed blue lines). The agreement between cross-correlations computed from the data and the simulations is striking. We fit a Gaussian curve to the radial profiles of the two-dimensional cross-correlations. At small scales ($<10'$) a $\sigma = 7.'7$ Gaussian profile is a good fit, and the result of the simulations agrees well with the data.

4. CALIBRATION USING CROSS CORRELATIONS

This paper uses four kinds of cross-power spectra, ACT × *WMAP*, ACT × ACT, $\mathrm{ACT}_{148} \times \mathrm{ACT}_{218}$, and *WMAP* × *WMAP* to provide CMB-based calibrations of the ACT maps. The advantage of working with the cross-power spectrum is that the noise in the two maps is independent and therefore uncorrelated. Hence a precise modeling of the noise is not needed.

If the noise in the two maps is uncorrelated, the cross-power spectrum provides an unbiased estimator of the underlying power spectrum. Cross-correlations can be done between pairs of maps from two different experiments. Because the two experiments have different systematics that do not correlate, the cross-spectrum provides a good estimate of the true underlying power spectrum that is nearly independent of the noise properties in the maps.

4.1. Power Spectrum Method

The power spectrum method we use is the Adaptive Multi-Taper Method (AMTM) of Das et al. (2009). Also we would like to have the maximum resolution possible in Fourier space to have as many bins in the power spectrum as possible, in order to maximize the number of independent measurements of the calibration factor as it is described below. The size of the bins is limited by the fundamental frequency determined by the smallest side of the maps. For the maps we are using, this is $\delta l = 72$. Using the AMTM with multiple tapers would result in smaller errors at the large l regime of the power spectrum, but it increases the size of the independent bins. For this reason we use AMTM with one taper at resolution $N\mathrm{res} = 1$ and thus no iterations are necessary (see Das et al. 2009 for the details of the AMTM method). We use slightly larger bin sizes than the fundamental frequency ($\delta l = 90$) to guarantee that the bins are uncorrelated. This is further tested and verified by Monte Carlo simulations. The prewhitening method of Das et al. (2009) is designed to reduce the dynamic range of the Fourier components of the maps. This is important when one is interested in measuring the damping tail of the CMB ($l > 1000$) where the slope of the power spectrum is steep. However, we do not use prewhitening as we are working in the mildly colored regime of the power spectrum, $l < 1000$ where the dynamic range of the power spectrum is not large. Using prewhitening does not affect the power spectrum at the l ranges of our interest. The point sources in the maps have a different spectral index than the CMB. In order to get an accurate calibration, it is important to identify and mask bright point sources in the maps before the power spectrum is computed. We mask the detected point sources of Marriage et al. (2011b) in our analysis.

The ACT power spectrum (both for 148 GHz and 218 GHz maps) is computed using cross-correlations of the four season maps. The power spectrum of each patch is the average of the

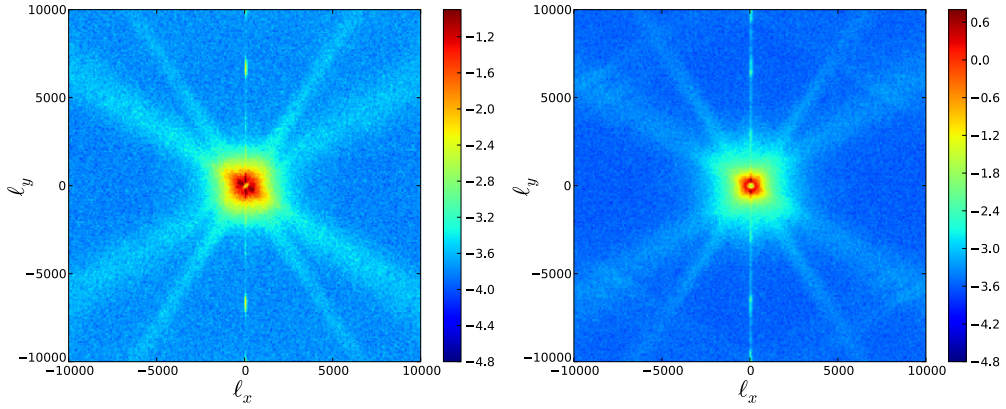

Figure 4. Average of 72 noise estimates (μK^2) in two dimensions for 148 GHz (left) and 218 GHz (right). Each estimate is computed from the auto-spectrum of a difference map obtained from differencing two quarter-season maps from the same region of the sky. The sky signal cancels in the difference maps and only noise remains. The anisotropy of the noise power spectrum is the reason we use these noise models to down-weight the noisy regions in two-dimensional power spectra before binning. These weights are different from those of Marriage et al. (2011a) in that the CMB is the main signal for us and it does not contribute to the noise model. The x and y are the right ascension and declination directions, respectively.

(A color version of this figure is available in the online journal.)

six cross-power spectra:

$$C_l^i = \frac{1}{6} \sum_{\alpha_i,\beta_i;\alpha_i<\beta_i}^{1\leqslant\beta_i\leqslant4} C_l^{\alpha_i\beta_i}, \tag{5}$$

where $C_l^{\alpha_i\beta_i}$ are cross-power spectra of season maps for the patch i, and α_i and β_i index the four season maps of that patch. The final ACT power spectrum is given by the average of the 12 patches:

$$C_l = \frac{1}{12} \sum_{i=1}^{12} C_l^i. \tag{6}$$

Each of these 12 power spectra is an independent measurement of the ACT power spectrum. We use the variance from the 12 power spectra values at each l bin as a measure of the error on the power spectrum. This method agrees well with the analytical estimate of the errors (Fowler et al. 2010).

The $\mathrm{ACT}_{148} \times \mathrm{ACT}_{218}$ cross-power spectrum is computed in a similar way, but in this case α_i and β_i correspond to the season maps from 148 GHz and 218 GHz data, respectively, and there are 12 cross-spectra for each patch:

$$C_l^i = \frac{1}{12} \sum_{\alpha_i,\beta_i;\alpha_i<\beta_i}^{1\leqslant\beta_i\leqslant4} \left(C_l^{\alpha_i\beta_i} + C_l^{\beta_i\alpha_i}\right). \tag{7}$$

The ACT $\times$ *WMAP* cross-power spectrum, C_l^{aw}, is given by the average of the 12-patch cross-power spectra. The spectrum in each patch is given by the average of the four cross-spectra between the *WMAP* map and each of the four ACT season maps for that patch,

$$C_l^i = \frac{1}{4} \sum_{\alpha_i=1}^{4} C_l^{\alpha_i}, \tag{8}$$

where α_i indexes the four season maps of the ith patch in ACT data and

$$C_l^{\alpha_i} = \frac{1}{N_l} \int d\theta \tilde{a}_{\alpha_i}(\boldsymbol{l})\tilde{w}^*(\boldsymbol{l}), \tag{9}$$

where N_l is the number of modes in each bin in Fourier space.

The window function deconvolution of the power spectra is done on the average cross-power spectrum of each patch. We have tested our pipeline on 1000 Monte Carlo simulations to confirm that the power spectrum method we use (including the two-dimensional noise weighting and the l-space masking) is unbiased and that the covariance matrix of the power spectrum bins is diagonal. The patch sizes used in Das et al. (2011) are three times larger than the patch sizes used in this paper, but the number of patches in Das et al. (2011) is three times fewer than that used here. So the total areas covered by both cutting methods are identical and for the same binning, the final power spectra obtained from the two methods agree with each other to better than 1% fractional error.

The straight binning of the two-dimensional power spectra is the simplest but not the best. Down-weighting noisy regions in the two-dimensional power spectrum space before binning is a useful technique that is adopted to improve the power spectrum method. Below we discuss our method for estimating the noise model and the two-dimensional noise weighting along with the l-space masking.

4.2. Noise Model

The season maps for each patch share the same signal but have independent noise properties. Differencing the two season maps removes the sky signal and leaves behind a linear combination of the noise in the two maps. The resulting map, which we call the "difference map," is a noise map and its auto-power spectrum can be used for estimating the noise model for that patch (see Marriage et al. 2011a for a more detailed discussion on noise weighting in Fourier space). Figure 4 shows the stacked noise models given by the average of 72 two-dimensional power spectra obtained from six difference maps per patch, for 12 patches.

4.3. Noise Weighting

The ACT and *WMAP* maps have very different noise properties. The *WMAP* noise spectrum is dominated by the detector noise and is nearly constant over a wide range of the wavevector l, whereas ACT noise has more detailed structure. The ACT noise is dominated by atmospheric noise on large angular scales, and by the detector noise on small scales. Some directions in the

two-dimensional ACT power spectrum are more noisy than others. We use our best estimate of the noise for each map to down-weight the noisy parts of the spectra before angle-averaging the two-dimensional spectra. The noise for the ACT–ACT cross-spectrum is $N^2_{aa}(\boldsymbol{l})$ and for the ACT–*WMAP* cross-spectrum it is $N_{aa}(\boldsymbol{l})N_{ww}(\boldsymbol{l})$, where $N_{aa}(\boldsymbol{l})$ is the ACT noise spectrum in two dimensions as shown in Figure 4 and $N_{ww}(\boldsymbol{l})$ is the *WMAP* noise. Noise weighted power spectra are then angle-averaged and binned in l. In the end, the spectra are divided by the beam and relevant pixel window functions. If we denote the two-dimensional spectra by $P(\boldsymbol{l})$, the final ACT–ACT cross-spectrum is obtained by

$$C^{aa}(l) = \frac{\int d\theta\, \tilde{P}_{aa}(\boldsymbol{l})/N^2_{aa}(\boldsymbol{l})}{F^2_c(l) b^2_a(l) \int d\theta / N^2_{aa}(\boldsymbol{l})}, \quad (10)$$

where $b_a(l)$ is the ACT beam in Fourier space (Hincks et al. 2010), $F_c(l)$ is the high-pass filter in Fourier space and $\int d\theta$ represents angle-averaging and binning in l. We do not correct for the ACT pixel window function as it is close to unity in the range of interest, $l < 1000$.

The ACT–*WMAP* cross-spectrum is obtained from

$$C^{aw}(l) = \frac{\int d\theta\, \tilde{P}_{aw}(\boldsymbol{l})/N_{aa}(\boldsymbol{l})}{F^2_c(l) b_a(l) b_w(l) p_w(l) \int d\theta / N_{aa}(\boldsymbol{l})}, \quad (11)$$

where $b_w(l)$ is the *W*-band beam of *WMAP* (Jarosik et al. 2011) and $p_w(l)$ is the pixel window function of the resolution 10 HEALPix maps corresponding to $N_{\rm side} = 1024$, with 3.′5 pixels. We use HEALPix in Python (healpy[35]) to compute the pixel window function at the integer harmonic indices and then bin it in l to get $p_w(l)$. The *WMAP* noise term gets canceled in the above noise weighting as it is constant.

We mask a vertical band of width $\Delta l_x = 180$ in the power spectra before angle-averaging them. This makes sure that our estimates of the power spectra are not affected by the striping effects that are present at a narrow band around $l = 0$. For this analysis, we use an l-space mask at $l_x = [-90, 90]$. For a detailed description of the l-space masking see Fowler et al. (2010).

4.4. Calibration: ACT 148 GHz

We assume that the calibration factor is constant on various scales and that the ACT, $a(x)$, and *WMAP*, $w(x)$, maps can be represented as

$$\begin{aligned} a(\boldsymbol{x}) &= \alpha^{-1} \Delta T_{\rm sky}(\boldsymbol{x}) \otimes B_a(\boldsymbol{x}) + N_a(\boldsymbol{x}), \\ w(\boldsymbol{x}) &= \Delta T_{\rm sky}(\boldsymbol{x}) \otimes B_w(\boldsymbol{x}) + N_w(\boldsymbol{x}), \end{aligned} \quad (12)$$

where α is the calibration factor (Dünner 2009), $\Delta T_{\rm sky}(\boldsymbol{x})$ is the sky temperature signal, N_a and N_w are ACT and *WMAP* noises, respectively, B_a is the ACT beam, and B_w is the *WMAP* beam. The calibration factor α appears in the cross- and auto-spectra of ACT, and it can be estimated through relevant ratios of the auto- and cross-spectra. We define

$$\begin{aligned} \alpha_1(l) &= C^{aw}_l / C^{aa}_l, \\ \alpha_2(l) &= C^{ww}_l / C^{aw}_l, \\ \alpha_3(l) &= \sqrt{\left(C^{ww}_l / C^{aa}_l\right)}, \end{aligned} \quad (13)$$

in which C^{ww}_l is the average 94 GHz (*W*-band) power spectrum of the *WMAP* seven-year data (*WMAP*7; Larson et al. 2011)[36] binned in the same way as the ACT auto- and cross-spectra. The calibration factors, α, are in fact estimators of the standard least-squares slope in Equation (12) on relevant angular scales. The three measures of the calibration defined in Equation (13) are not independent, but they have different systematics. α_1 and α_2 use cross-correlations of the two data sets, whereas α_3 only uses internal power spectra of ACT and *WMAP*. These three estimators can be used together to test the consistency of our results over a wide range of angular scales.

Variation of α versus l is a sign of a scale-dependent calibration factor. For the ACT 148 GHz maps, the calibration factor is constant in the range of $400 < l < 1000$, and different measures are consistent with each other within the errors. We restrict our analysis to this region. For $l \leqslant 300$ the ACT data are dominated by the atmospheric noise. Beyond $l > 1000$ *WMAP* maps are resolution limited.

The power spectrum bins are chosen such that the covariance between bins is negligible. Therefore, the ratios of the spectra, $\alpha(l)$, provide independent measurements of the calibration factor at every l bin. For the ACT 148 GHz maps the $\alpha(l)$ are flat over the range of $400 < l < 1000$. Hence, the overall calibration factor $\bar{\alpha}$ can be estimated from the average of the $\alpha(l)$ values in that l range. Since the covariance between the $\alpha(l)$ values at different l is negligible, the variance of the quantities that are used in averaging is a good measure of the error on the mean. Therefore we obtain

$$\begin{aligned} \bar{\alpha}_1 &= 1.01\% \pm 1.9\%, \\ \bar{\alpha}_2 &= 1.00\% \pm 2.1\%, \\ \bar{\alpha}_3 &= 1.00\% \pm 1.4\%. \end{aligned} \quad (14)$$

The uncertainties quoted are the error on the mean derived from the variance of the $\alpha(l)$ for every case. We use the Anderson–Darling statistic to test the normality of the $\alpha(l)$ measures. The A^2 statistic that quantifies deviations from normality in this test becomes large when data points deviate from normality. If $A^2 > 0.751$, the hypothesis of normality is rejected at the 95% confidence level (for a 90% confidence level it is 0.632). We compute A^2 for the three measures of the calibration factor defined above. The result is $A^2(\alpha_1) = 0.27$, $A^2(\alpha_2) = 0.26$, and $A^2(\alpha_3) = 0.43$. Therefore at the >10% level, the data used in computing the average calibration factor do come from a normal distribution.

Among the above three measures of the calibration factor, $\bar{\alpha}_3$ has the smallest error. The reason is that it uses the sky-averaged *WMAP* power spectrum as the estimate of the *WMAP* spectrum. Smaller errors in this quantity translate into the smaller error in the $\bar{\alpha}_3$. However, all three measurements are in agreement with each other. For comparison, the Uranus calibration is 0.99% ± 7.0%. We use 2% as the calibration error for the 148 GHz maps.

The calibrated power spectra are shown in Figure 5. The ACT 148 GHz–*WMAP* cross-spectrum is shown with blue filled circles, and single frequency spectrum of the ACT 148 GHz maps is shown with red triangles. The average 94 GHz (*W* band) power spectrum of the *WMAP* data binned in the same way as other spectra are binned (light green boxes) and the theory power spectrum based on *WMAP*7 best-fit parameters (solid black line) are also plotted for reference. The ACT × ACT power spectrum

[35] http://code.google.com/p/healpy

[36] http://lambda.gsfc.nasa.gov/product/map/dr3

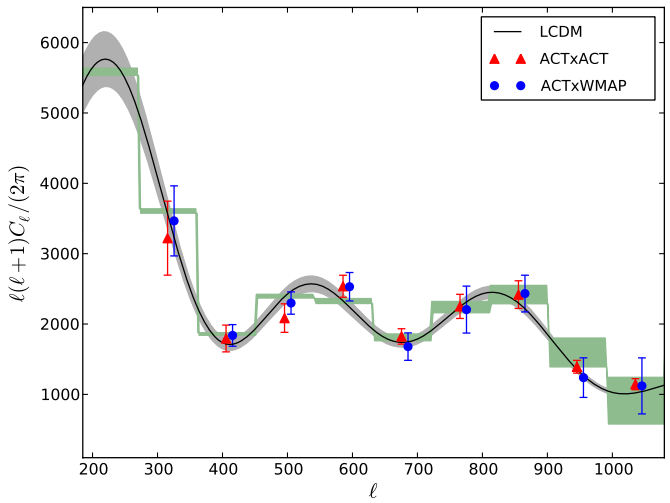

Figure 5. ACT × *WMAP* cross-power spectra. The ACT 148 GHz–*WMAP* cross-spectrum is shown with blue dots and the single frequency spectrum of the ACT 148 GHz maps is shown with red triangles. The average 94 GHz (*W* band) power spectrum of the *WMAP* data (light green squares) and the theory power spectrum based on *WMAP*7 best-fit parameters (solid black line) are also plotted for reference. The gray band shows the cosmic variance.

(A color version of this figure is available in the online journal.)

has large uncertainties on large scales due to the large-scale noise in the ACT maps. The *WMAP* power spectrum has larger errors on smaller scales where *WMAP* detector noise dominates and maps are resolution limited.

4.5. Calibration: ACT 218 GHz

We measure the calibration factor for the 218 GHz maps in a similar way. The result is a calibration factor with ∼7% fractional uncertainty in temperature. The larger uncertainty on the ACT 218 GHz calibration factor is due to the higher noise level in those maps than the 148 GHz maps on large angular scales. The calibration factors determined from cross-correlations with *WMAP* and from Uranus observations are consistent to ∼7%. We use 7% calibration error, based on Uranus, for the 218 GHz maps.

4.6. Calibration Systematics

Several factors can systematically affect our results.

1. *Stability versus time and space*. In order to examine the stability of our calibration results in time and space, we compare the average calibration factors in the 12 patches. The average α_l in every patch is computed by averaging the calibration factor for different l values in that patch. The scatter of the average calibration factors in 12 patches gives us a measure of stability of our results versus the position in the sky and the time that the patch was observed. We verify that the patch-to-patch variation of the calibration factor is consistent with the 1σ spread in the average calibration factor. We have also checked the independence of the calibration factor on the area of the map. The calibration factor measured on the 228 deg^2 data of Fowler et al. (2010) is the same as that measured on the ∼300 deg^2 map used in this work. An advantage of the calibration using cross-correlations is that the two data sets in the study are from the same region in the sky. Therefore, the cosmic variance does not affect the uncertainties on the calibration estimators that use cross-correlations.
2. *Beam uncertainty and window function normalization.* As discussed in Page et al. (2003), limited knowledge of the beam profiles leads to uncertainties in the experimental window function. These uncertainties result in a distortion of the power spectrum, which in turn affects our estimation of the calibration factor. One of the uncertainties is the uncertainty in the normalization of the ACT window function, which appears as an overall change in the calibration factor. The beam transfer function we use is normalized to unity at $l = 700$ and thus has no uncertainty at that l. The uncertainty in the beam transfer function is taken into account when estimating cosmological parameters (Dunkley et al. 2011) and we do not deal with it separately here.
3. *Pointing reconstruction error.* The error due to the pointing reconstruction is discussed in Jones et al. (2006) and causes a correlated distortion of the power spectrum at different bins. Absolute detector array pointings for the ACT data are established with 3.″5 precision through an iterative process in which the absolute pointing is adjusted based on offsets of ACT-observed radio source locations with respect to source locations taken from the Australia Telescope 20 GHz (AT20G) survey (Murphy et al. 2010). The bias induced by this error in the window function is not significant at the scales of our interest.
4. *The band center uncertainty.* Our calibration method is based on the CMB cross-correlations in two different frequencies. The CMB spectrum in the frequency range of this work is flat and therefore uncertainty in the frequency band center of the experiment will not affect our results.

5. COMBINING MAPS

The ACT and *WMAP* views of the CMB sky are complementary. *WMAP* accurately measures large-scale CMB features and ACT provides a high-resolution image of small-scale features. As we have shown in Sections 3 and 4, these maps are consistent and now cross-calibrated so that they can be combined to make a CMB map that is signal-to-noise dominated over a wide range of scales. The *WMAP* data are signal dominated on large scales, $l < 548$ (Larson et al. 2011), and the detector noise dominates at smaller scales. The ACT data are dominated by the unconstrained modes on large scales that arise from a combination of instrument properties, scan strategy, and atmospheric contamination. The ACT data have a good signal-to-noise ratio on intermediate scales, $500 < l < 5000$, and become noise dominated beyond that. The basics of our method for combining *WMAP* and ACT maps are similar to the real-space method described in Tegmark (1999). Working in real space has the disadvantage of having to deal with large matrices for large maps. Instead, we work in Fourier space. We construct a linear combination of the two maps in Fourier space by inverse noise weighting them such that the less noisy map dominates at each scale (these maps are not high-pass filtered). The *WMAP* data have lower angular resolution than ACT and the pixel size of *WMAP* is much bigger than that of ACT as well. We first deconvolve the *WMAP* data to the ACT angular resolution in Fourier space. Then we use inverse variance weighting to combine the two maps. The construction is given by

$$M(\boldsymbol{l}) = \frac{\sigma^2_{ww}(\boldsymbol{l})a(\boldsymbol{l})}{\sigma^2_{aa}(\boldsymbol{l}) + \sigma^2_{ww}(\boldsymbol{l})} + \frac{\sigma^2_{aa}(\boldsymbol{l})w(\boldsymbol{l})}{\sigma^2_{aa}(\boldsymbol{l}) + \sigma^2_{ww}(\boldsymbol{l})}, \quad (15)$$

where σ_{aa} and σ_{ww} are the ACT and *WMAP* noise spectra in two-dimensional Fourier space. The above combination picks

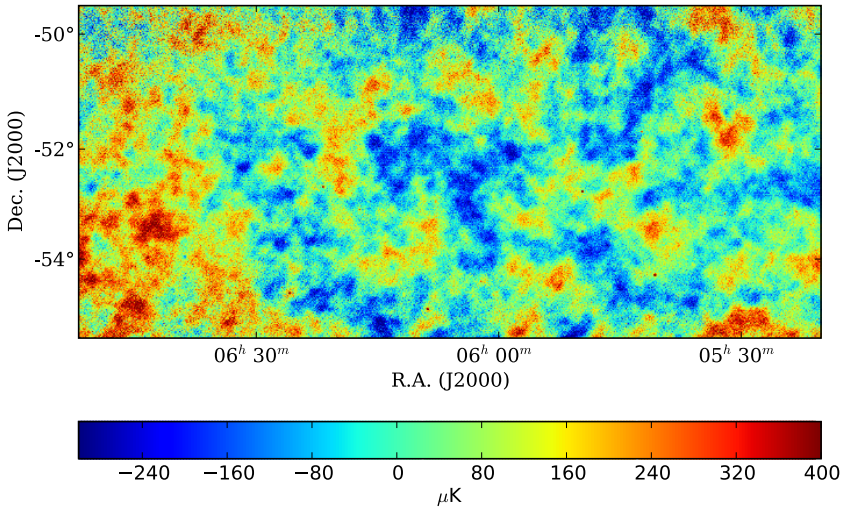

Figure 6. 84 deg^2 combined map obtained by combining *WMAP* and ACT 148 GHz maps. This high-resolution map encompasses all components of the microwave sky: the large-scale structure is the CMB, hot (red) dots are point sources, and some of the small cold (blue) spots are clusters of galaxies.
(A color version of this figure is available in the online journal.)

up *WMAP* contributions on large scales and ACT contributions on small scales and is signal dominated over a large range of l. The combined Fourier map, $M(\boldsymbol{l})$, is transformed back to real space. The ACT noise model, σ_{aa}, is computed in the same way as described above. *WMAP* noise is estimated by a white noise, i.e., a constant, before beam deconvolution. For beam-deconvolved *WMAP* maps, the noise model, σ_{ww}, is the *WMAP* noise multiplied by the two-dimensional beam window function in Fourier space. The resulting map is shown in Figure 6. This map encompasses all components of a high-resolution CMB map (CMB on large scales, point sources and clusters on small scales) in one single map.

6. CONCLUSION

We have presented a method for calibrating ACT maps using cross-correlations with *WMAP*. The fractional uncertainty in the temperature calibration factor obtained in this paper is $\sim$2% and the absolute calibration agrees well with that derived from Uranus observations. The calibration uncertainty is inversely proportional to the total area of the maps used for cross-correlations. Adding more area will decrease the uncertainty in the calibration factor. We have also presented fast methods for comparing and combining CMB data sets. Using these methods, we have combined ACT with *WMAP* data to construct a high-resolution map that has a good signal-to-noise ratio over a wide range of angular scales.

This work was supported by the U.S. National Science Foundation through awards AST-0408698 for the ACT project, and PHY-0355328, AST-0707731, and PIRE-0507768. Funding was also provided by Princeton University and the University of Pennsylvania. The PIRE program made possible exchanges between Chile, South Africa, Spain, and the United States that enabled this research program. Computations were performed on the GPC supercomputer at the SciNet HPC Consortium. SciNet is funded by the Canada Foundation for Innovation under the auspices of Compute Canada; the Government of Ontario; Ontario Research Fund—Research Excellence; and the University of Toronto.

A.H., V.A., S.D., and T.A.M. were supported through NASA grant NNX08AH30G. A.D.H. received additional support from a Natural Science and Engineering Research Council of Canada (NSERC) PGS-D scholarship. A.K. and B.P. were partially supported through NSF AST-0546035 and AST-0606975, respectively, for work on ACT. L.I. acknowledge partial support from FONDAP Centro de Astrofísica. R.D. was supported by CONICYT, MECESUP, and Fundación Andes. E.R.S. acknowledges support by NSF Physics Frontier Center grant PHY-0114422 to the Kavli Institute of Cosmological Physics. K.M., M. Hilton, and R.W. received financial support from the South African National Research Foundation (NRF), the Meraka Institute via funding for the South African Centre for High Performance Computing (CHPC), and the South African Square Kilometer Array (SKA) Project. J.D. received support from an RCUK Fellowship. R.H. received funding from the Rhodes Trust. We thank Norm Jarosik for useful discussions and his contributions. S.D. acknowledges support from the Berkeley Center for Cosmological Physics. Y.-T.L. acknowledges support from the World Premier International Research Center Initiative, MEXT, Japan. N.S. is supported by the U.S. Department of Energy contract to SLAC No. DE-AC3-76SF00515. We acknowledge the use of the Legacy Archive for Microwave Background Data Analysis (LAMBDA). Support for LAMBDA is provided by the NASA Office of Space Science. The data will be made public through LAMBDA (http://lambda.gsfc.nasa.gov/) and the ACT Web site (http://www.physics.princeton.edu/act/). Some of the results in this paper have been derived using the HEALPix (Górski et al. 2005) package.

REFERENCES

Abroe, M. E., Borrill, J., Ferreira, P. G., et al. 2004, ApJ, 605, 607
Battistelli, E. S., Amiri, M., Burger, B., et al. 2008, Proc. SPIE, 7020, 702028
Bennett, C. L., Hill, R. S., Hinshaw, G., et al. 2011, ApJS, 192, 17
Brown, M. L., Ade, P., Bock, J., et al. 2009, ApJ, 705, 978
Chiang, H. C., Ade, P. A. R., Barkats, D., et al. 2010, ApJ, 711, 1123
Crill, B. P., Ade, P. A. R., Artusa, D. R., et al. 2003, ApJS, 148, 527
Das, S., Hajian, A., & Spergel, D. N. 2009, Phys. Rev. D, 79, 083008
Das, S., Marriage, T. A., Ade, P. A. R., et al. 2011, ApJ, 729, 62
Dawson, K. S., Holzapfel, W. L., Carlstrom, J. E., Joy, M., & LaRoque, S. J. 2006, ApJ, 647, 13
Dunkley, J., Hlozek, R., Sievers, J., et al. 2011, ApJ, 739, 52
Dünner, R. 2009, PhD thesis, Pontificía Univ. Católica de Chile
Fowler, J. W., Acquaviva, V., Ade, P. A. R., et al. 2010, ApJ, 722, 1148
Fowler, J. W., Niemack, M. D., Dicker, S. R., et al. 2007, Appl. Opt., 46, 3444
Friedman, R. B., Ade, P., Bock, J., et al. 2009, ApJ, 700, L187

Ganga, K., Cheng, E., Meyer, S., & Page, L. 1993, ApJ, 410, L57
Górski, K. M., Hivon, E., Banday, A. J., et al. 2005, ApJ, 622, 759
Griffin, M. J., & Orton, G. S. 1993, Icarus, 105, 537
Hajian, A., & Souradeep, T. 2006, Phys. Rev. D, 74, 123521
Hernández-Monteagudo, C., Macías-Pérez, J. F., Tristram, M., & Désert, F. 2006, A&A, 449, 41
Hincks, A. D., Acquaviva, V., Ade, P., et al. 2010, ApJS, 191, 423
Hincks, A. D., Ade, P. A. R., Allen, C., et al. 2008, Proc. SPIE, 7020, 70201P
Hinshaw, G., Nolta, M. R., Bennett, C. L., et al. 2007, ApJS, 170, 288
Jarosik, N., et al. 2011, ApJS, 192, 14
Jones, W. C., Ade, P. A. R., Bock, J. J., et al. 2006, ApJ, 647, 823
Komatsu, E., Smith, K. M., Dunkley, J., et al. 2011, ApJS, 192, 18
Larson, D., Dunkley, J., Hinshaw, G., et al. 2011, ApJS, 192, 16
Lueker, M., Reichardt, C. L., Schaffer, K. K., et al. 2009, ApJ, 719, 1045
Marriage, T. A., Acquaviva, V., Ade, P. A. R., et al. 2011a, ApJ, 737, 61
Marriage, T. A., Baptiste Juin, J., Lin, Y.-T., et al. 2011b, ApJ, 731, 100
Marriage, T. A., Chervenak, J. A., & Doriese, W. B. 2006, Nucl. Instrum. Methods Phys. Res. A, 559, 551
Masi, S., Ade, P. A. R., Bock, J. J., et al. 2006, A&A, 458, 687
Mason, B. S., Pearson, T. J., Readhead, A. C. S., et al. 2003, ApJ, 591, 540
Menanteau, F., Gonzalez, J., Juin, J.-B., et al. 2010, ApJ, 723, 1523
Murphy, T., Sadler, E. M., Ekers, R. D., et al. 2010, MNRAS, 402, 2403
Netterfield, C. B., Devlin, M. J., Jarosik, N., Page, L., & Wollack, E. J. 1997, ApJ, 474, 47
Niemack, M. D. 2006, Proc. SPIE, 6275, 62750C
Niemack, M. D., Zhao, Y., Wollack, E., et al. 2008, J. Low Temp. Phys., 151, 690
Page, L., Barnes, C., Hinshaw, G., et al. 2003, ApJS, 148, 39
Reichardt, C. L., Ade, P. A. R., Bock, J. J., et al. 2009a, ApJ, 694, 1200
Reichardt, C. L., Zahn, O., Ade, P. A. R., et al. 2009b, ApJ, 701, 1958
Sayers, J., Golwala, S. R., Rossinot, P., et al. 2009, ApJ, 690, 1597
Sehgal, N., Bode, P., Das, S., et al. 2010, ApJ, 709, 920
Sehgal, N., Trac, H., Acquaviva, V., et al. 2011, ApJ, 732, 44
Sharp, M. K., Marrone, D. P., Carlstrom, J. E., et al. 2010, ApJ, 713, 82
Sievers, J. L., Mason, B. S., Weintraub, L., et al. 2009, arXiv:0901.4540
Sunyaev, R. A., & Zel'dovich, Y. B. 1970, Comments Astrophys. Space Phys., 2, 66
Swetz, D. S., Ade, P. A. R., Allen, C., et al. 2008, Proc. SPIE, 7020, 702008
Swetz, D. S., Ade, P. A. R., Amiri, M., et al. 2011, ApJS, 194, 41
Switzer, E. R., Allen, C., Amiri, M., et al. 2008, Proc. SPIE, 7019, 70192L
Tegmark, M. 1999, ApJ, 519, 513
Thornton, R. J., Ade, P. A. R., Allen, C., et al. 2008, Proc. SPIE, 7020, 70201R
Weiland, J. L., Odegard, N., Hill, R. S., et al. 2011, ApJS, 192, 19
Wright, E. L. 1976, ApJ, 210, 250
Xu, Y.-Z., Wu, X., & Soffel, M. 2001, Phys. Rev. D, 63, 103002
Zhao, Y., Allen, C., Amiri, M., et al. 2008, Proc. SPIE, 7020, 70200O